Letter Vol. 48, No. 21 / 1 November 2023 / Optics Letters 5819

Optics Letters

Wide-range OFDR strain sensor based on the femtosecond-laser-inscribed weak fiber Bragg grating array

Cailing Fu,[1,2] Ronglong Sui,[1,2] Zhenwei Peng,[1,2] Yanjie Meng,[1,2] Huajian Zhong,[1] Rongyi Shan,[1,2] Wenfa Liang,[1,2] Changrui Liao,[1,2] Xiaoyu Yin,[1,2] and Yiping Wang[1,2,3,*]

[1] Shenzhen Key Laboratory of Photonic Devices and Sensing Systems for Internet of Things, Guangdong and Hong Kong Joint Research Centre for Optical Fiber Sensors, State Key Laboratory of Radio Frequency Heterogeneous Integration, Shenzhen University, Shenzhen 518060, China

[2] Shenzhen Key Laboratory of Ultrafast Laser Micro/Nano Manufacturing, Key Laboratory of Optoelectronic Devices and Systems of Ministry of Education/Guangdong Province, College of Physics and Optoelectronic Engineering, Shenzhen University, Shenzhen 518060, China

[3] Guangdong Laboratory of Artificial Intelligence and Digital Economy (SZ), Shenzhen 518107, China

*ypwang@szu.edu.cn

Received 31 August 2023; revised 28 September 2023; accepted 16 October 2023; posted 17 October 2023; published 1 November 2023

A wide-range OFDR strain sensor was demonstrated based on femtosecond-laser-inscribed weak fiber Bragg grating (WFBG) array in standard SMF. A WFBG array consisting of 110 identical WFBGs was successfully fabricated along a 56 cm-long SMF. Compared with SMF, the cross-correlation coefficient of WFBG array was improved to 0.9 under the strain of 10,000 µε. The position deviation under the strain of 10,000 µε, i.e., 2.5 mm, could be accurately obtained and compensated simply by using peak finding algorithm. The maximum measurable strain of single- and multi-point strain sensing was up to 10,000 µε without using any additional algorithms, where the sensing spatial resolution was 5 mm.

https://doi.org/10.1364/OL.504763

An optical frequency domain reflectometer (OFDR) could be used to detect the changes of the external environmental, such as strain [1], temperature [2], and birefringence [3]. Among them, OFDR strain sensors have been widely used in three-dimensional shape sensing [4], structural health monitoring [5], and border security [6] due to their high-spatial resolution and high precision. However, in many cases, such as material fatigue testing [7] and geotechnical movement monitoring [8], an OFDR strain sensor with a wide measurement range, i.e., over 5000 µε, and a high-spatial resolution, i.e., mm-level, is required. To meet this demand, several algorithmic processing methods have been adopted to compensate for the position deviation induced by large strains [9–11]. For example, in 2018, an OFDR strain sensor with a measuring range of 3000 µε and a spatial resolution of 3 mm was realized using the local similarity of RS spectrum [12]. Subsequently, a combination of spectrum registration and spatial calibration was used to achieve a strain measurement range of 7000 µε at a spatial resolution of 5 mm [13]. Moreover, a strain of up to 10,000 µε was realized in a sweeping range of 40 nm based on recursive distance compensation method, where the spatial resolution was 2 mm [14]. Furthermore, the strain measurement range was extended to 10,000 µε at a length of 1 km by using a 20 nm splicing spectrum method, where the spatial resolution was 1 cm [15]. A wide-range phase-OFDR strain sensor with a measurement range of 14,000 µε was proposed using the phase accumulation method [16]. Although these algorithmic processing methods could be used to extend the strain measurement range, it brought huge computational burden to the already complex OFDR data processing process. A tunable laser with a large sweeping range is also required. On the other hand, the UV-laser-exposed SMF with enhanced RS could be also used to expand the strain measurement range from 800 to 2600 µε using the traditional method [17]. The strain sensing with a range of 50 µε was achieved using femtosecond-laser-processed 40 dB enhancement standard SMF in the 1 nm sweeping range [18]. However, the property of a wide-range strain sensing based on RS-enhanced fiber has not been reported yet.

In this Letter, a wide-range OFDR strain sensor was demonstrated based on femtosecond-laser-inscribed weak fiber Bragg grating (WFBG) array in standard SMF with an enhanced RS. A maximum measurable strain up to 10,000 µε was achieved over a sweeping range of 20 nm, where the sensing spatial resolution was 5 mm. The effects of generated new spectral components and position deviations caused by large strain on the similarity and sensing performance were studied. Moreover, the strain sensing properties of the SMF and WFBG array were further compared and investigated.

A conventional OFDR system was established for a wide-range strain sensing using femtosecond-laser-inscribed WFBG array, as shown in Fig. 1. The light from a tunable laser source (TLS, N7776C, Keysight) was divided into two parts by an optical coupler (OC_1) in a ratio of 10:90. The sweeping range and the sweeping rate of the TLS were 1548–1568 nm and 100 nm/s, respectively. Then the spatial resolution, i.e., Δz, could be calculated as 41.4 µm based on the equation $\Delta z = c/2n\Delta F$, where

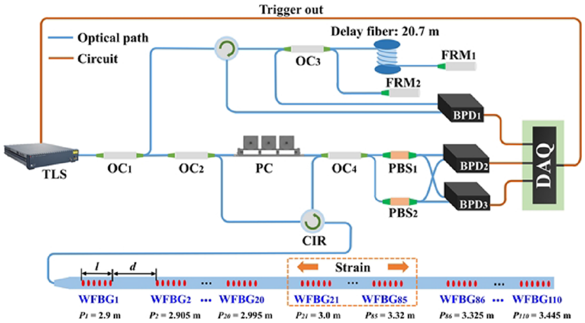

Fig. 1. Experimental setup for a wide-range strain sensing based on OFDR using femtosecond-laser-inscribed WFBG array. Note that the strain was applied in the area between the $WFBG_{21}$ and $WFBG_{85}$, corresponding to positions from 3.00 to 3.32 m. The length and spacing of WFBG are 1 mm and 4 mm, respectively, i.e., $l = 1$ mm, $d = 4$ mm. TLS, tunable laser source; OC, optical coupler; PC, polarization controller; FRM, Faraday rotation mirror; BPD, balanced photodetector; PBS, polarization beam splitter; CIR, circulator; DAQ, data acquisition card.

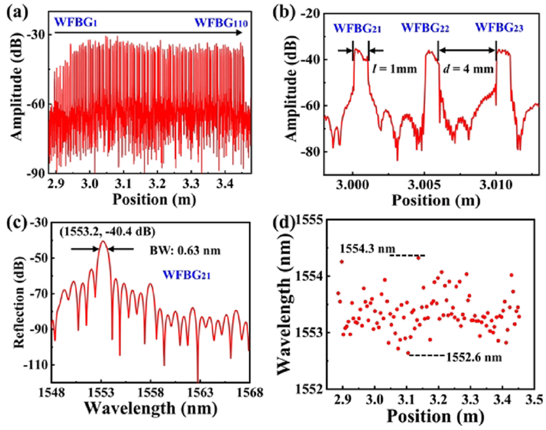

Fig. 2. (a) Obtained frequency domain spectrum of the femtosecond-laser-inscribed WFBG array in SMF, i.e., 110 identical WFBGs. (b) Amplified spectrum between $WFBG_{21}$ and $WFBG_{23}$. (c) Reflection spectrum of $WFBG_{21}$, corresponding to a reflectivity of 0.01%. (d) Distribution of Bragg wavelength for obtained WFBG array, ranging from 1552.6 to 1554.3 nm.

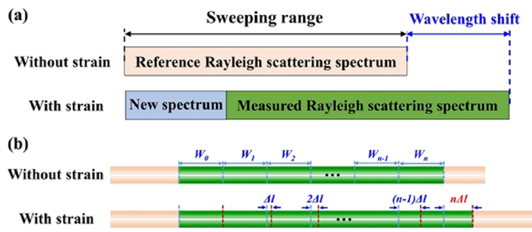

Fig. 3. (a) Comparison of reference (without strain) and measured (with strain) Rayleigh scattering (RS) spectrum. (b) Position deviation before and after applied strain, where the accumulated position deviation along the fiber is $n\Delta l$.

c, n, and ΔF are the light velocity in a vacuum, refractive index of the medium, and sweeping range of TLS. About 10% of the light was entered into an auxiliary interferometer (AI) of the Michelson structure, where the length of delay fiber is 20.7 m. The generated signal was used as the external clock of data acquisition card (DAQ,, PCI 6115, NI) to sample the beat signal from a balanced photodetector (BPD, PDB480C-AC, Thorlabs) at equidistant instantaneous optical frequency points. Two Faraday rotating mirrors (FRMs, Thorlabs), i.e., FRM_1 and FRM_2, in the AI are used to reduce the polarization fading effect [9]. The remaining 90% of the light was entered into the main interferometer of the Mach–Zehnder structure and divided by a 50:50 OC_2. Then the measured light, i.e., RS reflected by WFBG array, was mixed with the reference light, i.e., passing through the polarization controller (PC), through OC_4. Two polarization beam splitters (PBSs), i.e., PBS_1 and PBS_2, as well as two BPDs, i.e., BPD_2 and BPD_3, were employed to reduce the polarization fading effects in the MI.

Combining drag winding system with self-focusing process, an array consisting of 110 identical WFBGs were automatically inscribed in SMF using a femtosecond-laser point-by-point technology [19, 20]. Note that the pitch, length, and spacing of WFBG are 1.07 µm, 1 mm, and 4 mm, respectively. Among them, the $WFBG_1$ and $WFBG_{110}$ are located at 2.9 and 3.445 m, respectively, i.e., $P_1 = 2.9$ m, $P_{110} = 3.445$ m. As shown in Fig. 2(a), the average amplitude of the WFBG array was significantly enhanced from −67.2 to −35.48 dB. The measured position, length, and spacing of WFBG were consistent with the settings, as illustrated in Fig. 2(b). The reflectivity of $WFBG_{21}$ was −40.4 dB, i.e., 0.01%, where the Bragg wavelength and 3 dB-bandwidth were 1553.2 nm and 0.63 nm, respectively, as illustrated in Fig. 2(c). Obviously, the amplitude in Fig. 2(a), ranging from −53.6 to −30.6 dB, and Bragg wavelength in Fig. 2(d), ranging from 1552.6 to 1554.3 nm, exhibited a non-uniformity, which resulted from the fluctuation in femtosecond-laser pulse energies, the inhomogeneity in the core, and the positioning errors in image recognition process [20]. Fortunately, the non-uniformity has no effect on subsequent strain demodulation.

As shown in Fig. 3(a), when a fiber is subjected to strain, the RS spectrum not only exhibits a wavelength shift but also generates new spectral components. Then the overlap proportion between the reference (Ref.) and measured (Mea.) RS spectrum would be reduced, resulting in deteriorated similarity. Moreover, the similarity is deteriorated as the applied strain [12]. Assuming the applied strain is 10,000 µε, the wavelength shift can be calculated as 12.4 nm based on the strain sensitivity of 1.24 pm/µε. Therefore, the overlap proportion was less than 40%. On the other hand, position deviation is another factor that leads to deteriorated similarity. As shown in Fig. 3(b), the strain was applied to green section, which is divided into N windows, i.e., W_1, W_2, . . . , and W_n. Compared to the state without strain, the position of each window was deviated from the original position due to the elastic-optic effect. The position deviation induced by applied strain would be accumulated along the fiber, resulting in a position deviation of $n\Delta l$ for the last window.

To investigate the effect of deteriorated similarity on strain sensing performance, a strain of 10,000 µε was applied to a 32 cm length SMF and WFBG array. Two ends of SMF or WFBG array were fixed on two one-dimensional linear translation stages (XR25P, Thorlabs) via AB glue (DP460, 3 M). The strain was applied by moving one translation stage along the fiber axis. As shown in Fig. 1, the strain was applied in the area between the $WFBG_{21}$ and $WFBG_{85}$, corresponding to positions from 3.00 to 3.32 m. As shown in Fig. 4(a), there is an obvious

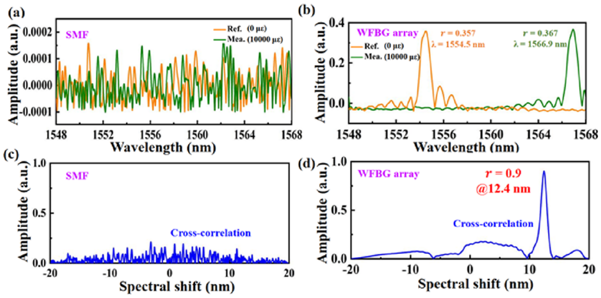

Fig. 4. Obtained reference, i.e., 0 με, and measured RS spectra, i.e., 10,000 με, of (a) SMF and (b) WFBG, labeled by orange and green curves, respectively; calculated cross-correlation results of (c) SMF and (d) WFBG. The cross-correlation coefficient of WFBG was improved to 0.9, where the wavelength shift induced by 10,000 με strain was 12.4 nm.

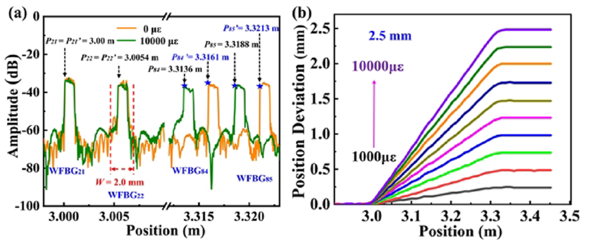

Fig. 5. (a) Schematic of the position of each WFBG under 0 and 10,000 με strains, labeled by orange and green curves, respectively. (b) Accumulated position deviation induced by applied strain, corresponding to 2.5 mm.

difference in the shape of the Ref. and Mea. spectrum for SMF, corresponding to the strain of 0 and 10,000 με, marked with orange and green curves, respectively. This indicated that new spectral components were generated, resulting in deteriorated similarity. Note that the reflection spectrum of WFBG is converted to the spectrum in a linear coordinate system to calculate the cross-correlation spectral shift. As shown in Fig. 4(c), the cross-correlation peak could not be identified due to deteriorated similarity induced by small overlap proportion illustrated in Fig. 3(a). Thus, the deteriorated similarity induced by a new spectrum under a large strain made it impossible for SMF to achieve a large strain sensing. For the WFBG array, the Ref. and Mea. spectrum have the same spectral shape but different Bragg wavelengths, corresponding to a wavelength of 1554.5 nm and 1566.9 nm, respectively, as shown in Fig. 4(b). This indicated that the WFBG array with enhanced RS could still maintain good similarity under large strain. Compared with SMF, the cross-correlation coefficient of WFBG could be improved to 0.9, where the cross-correlation spectral shift was 12.4 nm, as shown in Fig. 4(d). Note that cross-correlation algorithm was used to calculate the spectral shift attributing to its tiny wavelength error.

Moreover, the position deviation induced by large strain could be also compensated by using the WFBG array. As shown in Fig. 5(a), the positions of $WFBG_{21}$ and $WFBG_{22}$ were completely coincided under the strain of 0 and 10,000 με. But at the end of the strain region, the positions of $WFBG_{84}$ and $WFBG_{85}$ were deviated from 3.3136 and 3.3188 to 3.3161 and 3.3213 m, respectively. As shown in Fig. 5(b), the position deviation was increased from 0.24 to 2.5 mm. This indicated that the position

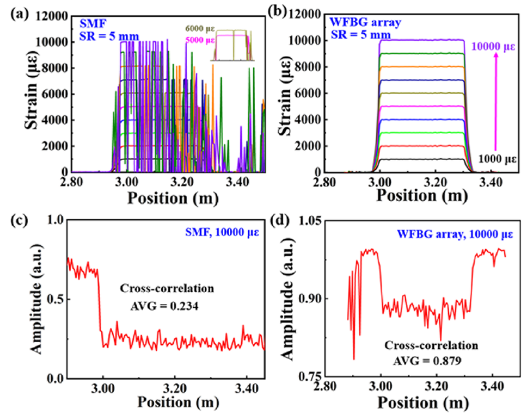

Fig. 6. Demodulated strain profiles based on (a) SMF and (b) WFBG array, when the applied strain was increased from 1000 to 10,000 με with a step of 1000 με under a spatial resolution of 5.0 mm; calculated cross-correlation coefficient amplitude along the (c) SMF and (d) WFBG array under the strain of 10,000 με, corresponding to the average values of 0.234 and 0.879, respectively.

of each WFBG in the array before and after strain could be accurately obtained by use of peak finding algorithms in the distance domain. Note that the length of the window is 2 mm, i.e., $W = 2$ mm. In this way, the position deviation induced by a large strain illustrated in Fig. 3(b) could be well compensated. Therefore, the deteriorated similarity induced by generated new spectrum and position deviation under large strains could be completely addressed by femtosecond-laser-inscribed WFBG array.

The strain sensing properties of the SMF and WFBG array were further compared and investigated, when the strain was increased from 1000 to 10,000 με with a step of 1000 με. As shown in Fig. 6(a), the strain for SMF could be clearly demodulated, when the strain was less than 6000 με. However, the strain signal was submerged in noise, when the applied strain was greater than 6000 με. Note that the sensing spatial resolution is set to 5 mm in the strain demodulation, which is the length of the WFBG, i.e., $l = 1$ mm, plus the spacing, i.e., $d = 4$ mm. In contrast, the applied strain for the WFBG array could be clearly identified without fluctuation, as illustrated in Fig. 6(c). This indicated that the sensing performance was greatly improved by using femtosecond-laser-inscribed WFBG array. Moreover, the average cross-correlation coefficient of the WFBG array in the strain-applied area, i.e., between 3.00 and 3.32 m, is as high as 0.879, under the strain of 10,000 με, as shown in Fig. 6(d). Compared with WFBG array, the average cross-correlation coefficient of SMF is reduced to 0.234, as illustrated in Fig. 6(b). Obviously, the cross-correlation coefficient of SMF in the zero-strain area at the back end, i.e., 3.32 m away, was influenced by the previous strain-applied area, resulting in the same low cross-correlation coefficient as the previous strain-applied area. But for the WFBG array, the cross-correlation coefficient remained at 1 in the two areas between 2.90 to 2.995 m and 3.325 to 3.46 m, i.e., zero-strain area.

To further verify the multi-point strain sensing performance of the WFBG array, the strain was applied simultaneously to two areas at different positions, i.e., 3.0 to 3.11 m and 3.33 to 3.44 m. As shown in Fig. 7, the strains in both strain-applied areas, middle zero-strain, and rear-end zero-strain were successfully and clearly demodulated, when the strain was increased from 1000 to 10,000 με with a step of 1000 με. This phenomenon

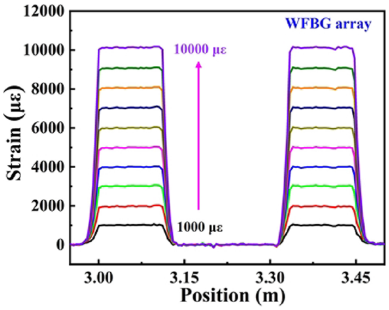

Fig. 7. Demodulated multi-point strain profile based on WFBG array, when the applied strain was increased from 1000 to 10,000 με under a sensing spatial resolution of 5 mm.

further indicated that femtosecond-laser-inscribed WFBG arrays with enhanced RS could effectively eliminate the deteriorated similarity induced by a large strain. Moreover, multiple-channel WFBG arrays with different Bragg wavelengths could also be used for multiple-channel strain sensing. In addition, the total response time for a wide-range strain sensing is approximately 1.5 s, including sweeping time of 0.5 s, return time of 0.178 s, and data processing time, i.e., 0.8 s, which could be improved by using GPU [21].

In conclusion, a wide-range OFDR strain sensor, i.e., up to 10,000 με, was demonstrated based on the femtosecond-laser-inscribed WFBG array in standard SMF, where the sensing spatial resolution was 5 mm. The average amplitude of the obtained WFBG array, consisting of 110 identical WFBG, was enhanced about 31.72 dB. The deteriorated similarity induced by generated new spectrum and position deviation under large strains could be completely addressed by femtosecond-laser-inscribed WFBG array. Compared with SMF, the cross-correlation coefficient of the WFBG array was improved to 0.9 under the strain of 10,000 με. Moreover, the position deviation under the strain of 10,000 με, i.e., 4 mm, could be well compensated. The single- and multi-point strain applied for the WFBG array could be clearly identified without fluctuation, when the applied strain was increased from 1000 to 10,000 με.

Funding. National Key Research and Development Program of China (2022YFE0111400); National Natural Science Foundation of China (U1913212, U22A2088); Guangdong Science Technology Department (2021A1515011925); Shenzhen Science and Technology Program (JCYJ20200109114020865, JCYJ20200109114201731, JCYJ20200810121618001, JSGG20201102152200001); Shenzhen Key Laboratory of Ultrafast Laser Micro/Nano Manufacturing (ZDSYS20220606100405013).

Disclosures. The authors declare no conflicts of interest.

Data availability. Data underlying the results presented in this paper are not publicly available at this time but may be obtained from the authors upon reasonable request.

REFERENCES

1. J. Li, J. Gan, Z. Zhang, X. Heng, C. Yang, Q. Qian, S. Xu, and Z. Yang, Opt. Express **25**, 27913 (2017).
2. H. Zhong, C. Fu, P. Li, B. Du, C. Du, Y. Meng, and Y. Wang, Opt. Lett. **47**, 882 (2022).
3. Z. Ding, C. Wang, K. Liu, Y. Liu, G. Xu, J. Jiang, Y. Guo, and T. Liu, Opt. Express **27**, 951 (2019).
4. C. Fu, Y. Meng, L. Chen, H. Zhong, C. Du, J. He, X. Weng, L. Liu, J. Qu, and Y. Wang, Opt. Lett. **48**, 3219 (2023).
5. P. Zhu, X. Xie, X. Sun, and M. A. Soto, Composites, Part B **168**, 267 (2019).
6. Z. Yao, T. Mauldin, Z. Xu, G. Hefferman, and T. Wei, Opt. Lett. **45**, 6086 (2020).
7. M. T. A. Ansari, K. K. Singh, and M. S. Azam, J. Reinf. Plast. Compos. **37**, 636 (2018).
8. C.-Y. Hong, Y.-F. Zhang, M.-X. Zhang, L. M. G. Leung, and L. Q. Liu, Sens. Actuators, A **244**, 184 (2016).
9. P. Li, C. Fu, B. Du, J. He, H. Zhong, C. Du, L. Wang, and Y. Wang, J. Lightwave Technol. **39**, 6334 (2021).
10. K. Feng, J. Cui, H. Dang, D. Jiang, Y. Jin, X. Sun, and X. Zhang, IEEE Photonics Technol. Lett. **31**, 1108 (2019).
11. C. Wang, K. Liu, Z. Ding, J. Jiang, Z. Chen, Y. Feng, Y. Zheng, Q. Liu, and T. Liu, J. Lightwave Technol. **38**, 5825 (2020).
12. K. Feng, J. Cui, D. Jiang, H. Dang, Y. Jin, X. Sun, Y. Niu, and J. Tan, Opt. Lett. **43**, 3293 (2018).
13. S. Qu, Z. Qin, Y. Xu, Z. Cong, Z. Wang, and Z. Liu, J. Lightwave Technol. **39**, 6340 (2021).
14. S. Qu, Z. Wang, Z. Qin, Y. Xu, Z. Cong, and Z. Liu, IEEE Internet of Things J. **9**, 2882 (2022).
15. T. Zhu, C. Lin, J. Yang, Z. Yu, P. Xu, K. Wen, Y. Wang, and Y. Qin, Opt. Express **31**, 20980 (2023).
16. M. Wang, W. Feng, K. Xie, H. Jia, J. Lin, and G. Tu, J. Lightwave Technol. **40**, 5307 (2022).
17. C. Du, C. Fu, P. Li, Y. Meng, H. Zhong, B. Du, K. Guo, L. Chen, Y. Wang, and J. He, J. Lightwave Technol. **41**, 1566 (2023).
18. Q. Wang, K. Zhao, M. Badar, X. Yi, P. Lu, M. Buric, Z.-H. Mao, and K. P. Chen, IEEE Sens. J. **22**, 18471 (2022).
19. YOFC, "Single mode optical fiber," 2021, https://www.yofc.com/view/864.html.
20. B. Xu, J. He, B. Du, X. Xiao, X. Xu, C. Fu, J. He, C. Liao, and Y. Wang, Opt. Express **29**, 32615 (2021).
21. C. Wang, K. Liu, Z. Ding, Y. Li, D. Zhu, M. Pan, Z. Chen, H. Guo, S. Li, J. Jiang, Y. Yu, and T. Liu, IEEE Sens. J. **21**, 24166 (2021).